Two-Dimensional Tomographic Simultaneous Multi-Species Visualization—Part I: Experimental Methodology and Application to Laminar and Turbulent Flames

Thomas Häber [1],* , Henning Bockhorn [2] and Rainer Suntz [1]

[1]   Institute of Chemical Technology and Polymer Chemistry, Karlsruhe Institute of Technology (KIT), 76131 Karlsruhe, Germany; rainer.suntz@kit.edu

[2]   Engler-Bunte-Institute, Chair of Combustion Technology, Karlsruhe Institute of Technology (KIT), 76131 Karlsruhe, Germany; henning.bockhorn@kit.edu

*   Correspondence: thomas.haeber@kit.edu

Abstract: In recent years, the tomographic visualization of laminar and turbulent flames has received much attention due to the possibility of observing combustion processes on-line and with high temporal resolution. In most cases, either the spectrally non-resolved flame luminescence or the chemiluminescence of a single species is detected and used for the tomographic reconstruction. In this work, we present a novel 2D emission tomographic setup that allows for the simultaneous detection of multiple species (e.g., OH*, CH* and soot but not limited to these) using a single image intensified CCD camera. We demonstrate the simultaneous detection of OH* (310 nm), CH* (430 nm) and soot (750 nm) in laminar methane/air, as well as turbulent methane/air and ethylene/air diffusion flames. As expected, the reconstructed distributions of OH* and CH* in laminar and turbulent flames are highly correlated, which supports the feasibility of tomographic measurements on these kinds of flames and at timescales down to about 1 ms. In addition, the possibilities and limitations of the tomographic approach to distinguish between locally premixed, partially premixed and non-premixed conditions, based on evaluating the local intensity ratio of OH* and CH* is investigated. While the tomographic measurements allow a qualitative classification of the combustion conditions, a quantitative interpretation of instantaneous reconstructed intensities (single shot results) has a much greater uncertainty.

Keywords: optical emission tomography; combustion; chemiluminescence; tomographic reconstruction algorithms; Tikhonov regularization; laminar diffusion flame; turbulent diffusion flame; local equivalence ratio

1. Introduction

Modern gas turbines are operated under lean fuel conditions to reduce NOx emissions, sometimes producing unstable operating conditions. Such instabilities are characterized by periodic fluctuations in the total volumetric heat release, which lead to considerable pressure fluctuations within the combustion chamber. As a result, on the one hand, unacceptable noise pollution occurs in the area around the power plant. On the other hand, high mechanical loads on the parts of the combustion device, especially at the blades of the high-pressure turbine, are induced. In order to avoid these unstable operating conditions, an easily accessible measurement signal is required that correlates with the heat release rate of the flame. This signal can then be used for online process control to avoid these unstable operating conditions, e.g., by varying the fuel supply.

In hydrocarbon flames, electronically excited radicals, such as CH* ($A^2\Delta$, $B^2\Sigma^-$), OH* ($A^2\Sigma^+$), C_2* ($d^3\Pi_g$), HCO* (A^2A'', B^2A'), CO* ($A^1\Pi$, $d^3\Delta$, $a^3\Pi$) and CO_2* (A^1B_2) are generated by highly exothermic reactions [1]. The concentrations of these electronically excited species in the reaction zone of fuel-air flames far exceed their thermal equilibrium values [1]. The chemiluminescence (CL) of these species is a natural probe for the progress of the combustion process. Due to its simplicity compared to modern but much more complex and cost intensive laser techniques, such as LIF (laser-induced fluorescence) or Rayleigh/Raman scattering, the use of chemiluminescence in combustion research has attracted increasing interest over the past decades. For example, it was found that the chemiluminescence of OH* in premixed laminar and moderately turbulent hydrocarbon flames correlates with the heat release rate [2–5], which is the dominant physical quantity of combustion processes and considerably determines their stability [3]. In addition, various studies have shown that certain ratios of the chemiluminescence intensities (e.g., CH*/OH* [2,6–12] and C_2*/OH* [5,6,8,9]) are a measure of the equivalence ratio in premixed flames [2,5,7–10,12] and a marker to determine the quality of mixing in premixed or the local stoichiometry in partially-premixed zones of diffusion controlled combustion in turbulent flames [11,13]. Therefore, monitoring the chemiluminescence is a valuable tool for the non-invasive diagnostic of industrial combustion processes.

Compared to 1D or 2D laser-based techniques, chemiluminescence signals are usually subject to line-of-sight integration and, hence, lack some of the spatial information. For example, in References [14,15] heat release rates in turbulent premixed ethylene-air flames were obtained using three different methods: (1) simultaneous two-dimensional CH_2O- and OH-LIF, (2) flame surface density method and (3) OH* chemiluminescence. The authors were able to show that line-of-sight integrated images of OH* provide qualitative information about the heat release rate but compared to the other methods, no local values can be determined. Novel optical methods must, therefore, be used for the detection of spatially resolved chemiluminescence distributions, such as Cassegrain telescopes coupled to a spectrograph or photomultipliers equipped with bandpass filters [2,6,8,9,13,16–19]. These systems were successfully used to investigate the behavior of chemiluminescence signals for a broad range of combustion conditions. However, Cassegrain-based methods are single point measurements, which makes it difficult to apply them to dynamic processes in space and time. In addition, the contamination of the chemiluminescence signals by emissions originating from regions outside the sample volume and along the propagation direction of the measurement signal cannot be ruled out.

Optical emission tomography avoids most of these disadvantages. It facilitates the detection of 2D or even 3D distributions of the chemiluminescence emission from laminar and turbulent hydrocarbon flames of any geometry. The development and application of tomographic methods for the reconstruction of 2D [20–22] and 3D [23–45] flame structures in laminar [21,22,24,28–30,33,39–42] and turbulent [20,23,25–27,30–32,34–37,43–45] flames have gained a lot of interest in the past decade. They are used to image the distribution of chemiluminescent species [20–25,28,29,31–35,37–50] or the volumetric OH-LIF signal [26,27,30,51], as well as the 3D flow field using tomographic particle image velocimetry (tomo PIV) [52–56]. More recently the focus has shifted towards space- and time-resolved tomographic measurements with kHz-repetition rate [25,27,32,34,35,42,44,45], for example to obtain time and space resolved Rayleigh index fields in swirl-stabilized flames [25,44]. A significant disadvantage in this context is the very high investment costs for installing up to ten high-speed cameras, preferably with image intensifiers, in order to be able to detect the extremely weak chemiluminescence signal at exposure times of less than 1 ms. For reference, the concentration of OH* is in the ppb-range and several orders of magnitude lower (5 to 6 orders of magnitude) compared to that of OH originating from the chain branching reaction [57–59]. Due to the low signal intensity, the imaging optics and optical resolution in each tomographic setup are a compromise between the desired spatial resolution and an adequate signal-to-noise ratio for the detection of the radon projections. In general, the spatial resolution of the tomographic methods is inferior compared to, e.g., the Cassegrain-based point

measurements, but they provide the complete 2D or 3D distribution within a single image, which is necessary for the investigation of dynamic processes in space and time.

To reduce the costs of the tomographic setup, different systems have been developed that reduce the number of cameras, while maintaining the same number of projection angles. One possibility is to use a special mirror-based relay optic between the flame and the camera, which maps several 2D projections onto each camera, but it still requires three or more cameras [25–27,30,42,44,45]. The other option uses a customized bundle of optical fibers to project the chemiluminescence onto the camera sensor [20,21,28,29,32,34,41]. Anikin et al. were the first to work with a fiber bundle and to demonstrate the 2D tomographic imaging of laminar and turbulent flame structures with a single image intensified camera [20,21]. The fiber bundle consisted of 10 legs, each with 90 fibers (arranged side by side in a row), which were brought together in a common fiber ferrule and imaged onto the camera via a customized relay optic. Later Hossain et al. extended the approach to image 3D flame structures using two fiber bundles and two cameras, with eight projection angles and 7500 optical fibers per angle [28,29]. Recently, Liu et al. demonstrated kHz-rate volumetric flame imaging using a single camera and a fiber bundle with nine legs [32]. They also extended the setup by two more cameras and up to a total number of 17 projection angles, to increase the spatial resolution and reconstruction quality [34].

In this work, we present a novel extension (POET$^\lambda$) of our planar emission tomograph (POET) that enables the simultaneous detection of multiple wavelengths/species in laminar and turbulent flames using a single image-intensified camera. We demonstrate the simultaneous detection of OH* (310 nm), CH* (430 nm) and soot (750 nm) in laminar methane/air, as well as turbulent methane/air and ethylene/air diffusion flames.

The presentation of the results has been split into two parts. The first part (Part I is this paper) describes the methodology, the experimental setup and the validation of the multi-species detection using non-sooting and sooting diffusion flames under laminar and turbulent conditions. In addition, we will investigate possibilities and limitations of the tomographic approach to distinguish between locally premixed, partially premixed and non-premixed conditions, based on evaluating the local intensity ratio of OH* and CH*.

In Part II, we will take advantage of the strong spatial (and temporal) coupling of OH* and CH* in laminar and moderate turbulent flames. Multi-species tomography enables us to quantify the reconstruction quality completely independent of any phantom studies instantaneously. This is especially important in turbulent flames, where it is difficult to separate measurement noise from turbulent fluctuations. Thus, in Reference [60] we present a detailed analysis and comparison of different reconstruction algorithms. It has been shown that reconstruction methods based on Tikhonov regularization should be preferred over the widely used algebraic reconstruction technique (ART) and multiplicative algebraic reconstruction techniques (MART), especially for high-speed imaging of turbulent flames or generally in the limit of low signal-to-noise ratio.

2. Materials and Methods

2.1. Burner

The measurements presented here were carried out in laminar and on turbulent diffusion flames. The burner was the same as in our previous work [20]. It is similar to that in References [14,15] except for a smaller plenum and the use of a perforated plate instead of the flow straightener to unify the flow field (Figure 1). The burner had an annular opening with an inner diameter of 25 mm and an outer diameter of 35 mm. Air entered the burner from the side, flowed through the perforated plate and exited the burner through the annular opening. The fuel was supplied through six radial bores in the centrally arranged conical bluff-body. The bores had a diameter of 0.7 mm and were located 2 mm below the bluff-body edge. The turbulence intensity was estimated previously to be ≈10% of the inlet velocity [20]. Thermal mass flow controllers (MKS Instruments) controlled the mass flow rates of fuel

and air. All gases entered the burner at room temperature. The mass flow of fuel (methane or ethylene) in most measurements was in the range of 1–2 slm (standard liter per minute), while the air flow was varied from 10 slm (laminar case) to 100 slm (turbulent case), resulting in an exit velocity of the fuel/air mixture of about 0.4 or 3.6 m/s, respectively.
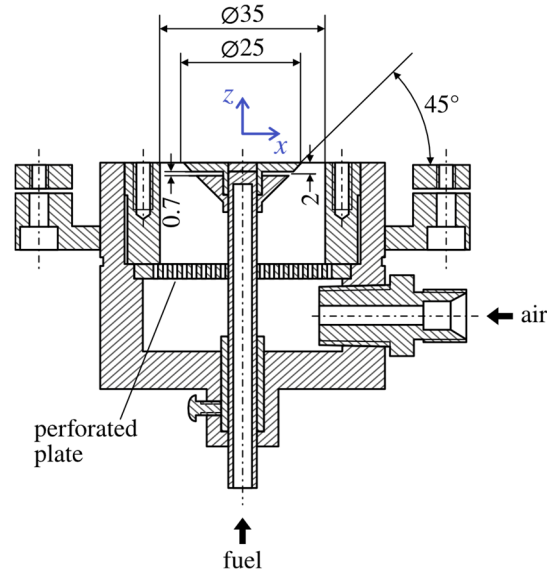

**Figure 1.** Axial cross-section of the diffusion flame burner [20].

2.2. Tomographic Setup, POET$^\lambda$

The wavelength selective planar optical emission tomograph (*POET$^\lambda$*) consisted of ten telescopes arranged in a semi-circle around the burner (Figure 2). As in our first version of the tomograph (POET) [21], the flame emission was deflected into the vertical direction by UV-enhanced aluminum mirrors mounted at an angle of 45° on top of each telescope, which projected the light onto a row of optical fibers. The telescopes performed two important functions: (1) They ensured that each optical fiber detected the luminescence signal only at a small solid angle in space and (2) they mapped the field of view (64 mm) to the length of a fiber row, with a reduction factor of 5.7. All ten fiber rows were bundled into a single ferrule and the emitted light was imaged onto a single intensified CCD camera (ICCD, PIMAX-4 1024f, Princeton Instruments). Each leg of the fiber bundle (Ceram Optec SIA) contained 102 fused silica fibers (NA 0.22, core ø100 µm, outer ø125 µm) densely packed and arranged side by side in a row. On the telescope side, the polyimide jacket had been removed from the fibers to allow for a denser packing of the bare fibers (ø110 µm) and, hence, a better optical resolution with a total length of each fiber row of 11.22 mm (102 × 110 µm). On the camera side, the protective jacket was retained in order to ensure enough spatial separation of the signals of neighboring fibers on the camera sensor.

In the following, the definition of the coordinate systems was used as depicted in Figures 1 and 2a: The coordinate system was centered in the middle of the flame or the measurement region, with the *z*-axis oriented perpendicular to the horizontal measurement plane. The acute angle between the *x*-axis and the projection directions of telescopes 1 and 10 was 9°. The *y*-axis lay in the middle between projection directions 5 and 6. In addition, a local coordinate system was used for the telescopes, in which the *µ*-axis lay in the projection direction (line-of-sight) and the *v*-axis was perpendicular to the *µ*- and *z*-axes.

In our previous single-wavelength setup (POET) [20,21], the telescopes used a Kepler design with two plano-convex quartz glass lenses (*f* = 75 mm and 500 mm) and an iris aperture (ø15 mm) in the focal plane of both lenses to the detection to a small solid angle. However, especially the small short focal length lens caused strong chromatic aberrations in multi-wavelength operation. As a

result, the OH* (310 nm) and CH* (430 nm) focal planes were displaced by ~120 mm relative to each other in the projection direction (line-of-sight), resulting in unacceptably different optical resolutions (in-plane and out-of-plane, see below) of both wavelengths. In the current setup (Figure 3), chromatic aberrations were minimized by using a spherical concave mirror instead of the short focal length lens. In order to minimize geometric aberrations, the concave mirror was inclined only by 6° with respect to the optical axis of the large, long focal length lens, which resembled a variant of the Herschelian reflector [61]. A small deflecting mirror then directed the light onto the fiber ferrule and the row of optical fibers. Using the clear aperture of the top lens ($D = 66$ mm) and its distance to the burner matrix ($f = 478$ mm), the $f_\#$-number of the telescope was calculated to be $f_\# = f/D \approx 7.2$.
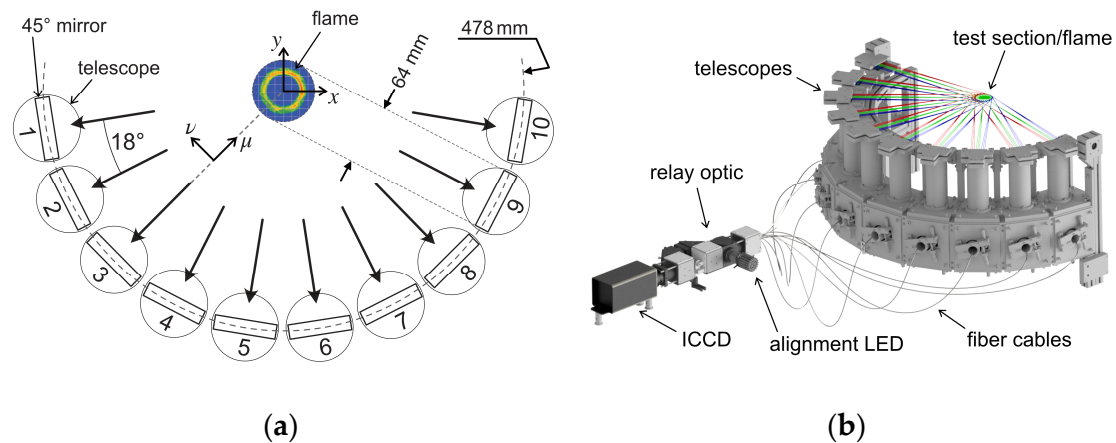

Figure 2. (**a**) Schematic illustration of the tomographic setup (POET$^\lambda$). The emission of the flame was imaged by ten 45° deflection mirrors and suitable telescopes onto individual rows of optical fibers. (**b**) 3D illustration of telescopes, optical fiber cables, relay optic and camera.
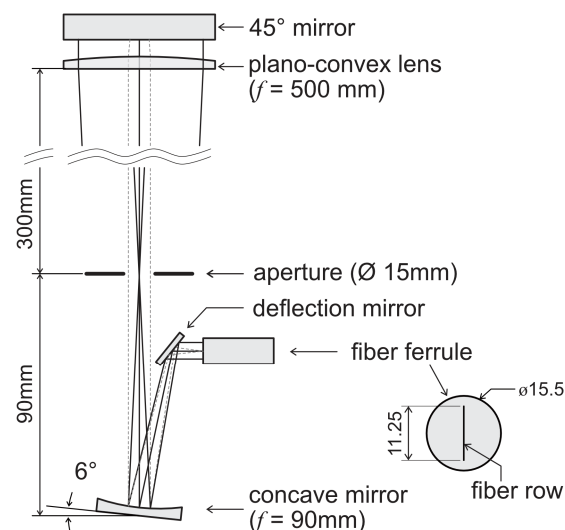
Figure 3. Schematic illustration of the optical setup of the telescopes. Using a concave mirror instead of a plano-convex lens minimizes chromatic aberrations in multi-wavelength operation.

To estimate the imaging performance of the telescopes, ray-tracing simulations were performed with our in-house code [62]. Light rays were traced back from the optical fibers to determine the sample volume imaged by each fiber. For each fiber, 10^6 rays were traced, which were uniformly distributed over the cross-section of the fiber and left/entered the fiber with a numerical aperture of Na $\approx 0.5/f_\# = 0.07$. Figure 4a shows the variation of the out-of-plane resolution (vertical to the measurement plane) over the depth of the interrogation region for (i) the old telescope (dashed lines), consisting of two plano-convex

lenses, and (ii) the new design (solid lines), in which the short focal length lens has been replaced by a spherical concave mirror. The horizontal axis corresponds to the line-of-sight direction of the telescopes. Selected intensity profiles $I(v,z)$ of the imaged volumes/cross-sections at the marked points A, B, C, and D are shown in Figure 4b. The spot height (resolution) is defined as the height which contains 76% of the total intensity. For a Gaussian intensity profile, this would exactly match the full width at half-maximum (FWHM). The white lines illustrate the shape of the cumulative probability density curves along the z-axis, vertical to the measurement plane, $CDF(z) = \int_{-\infty}^{z} \int_{-\infty}^{+\infty} I(v, z\prime)dvdz\prime$, where $I(v,z)$ is the intensity profile.


(a)   **(b)**
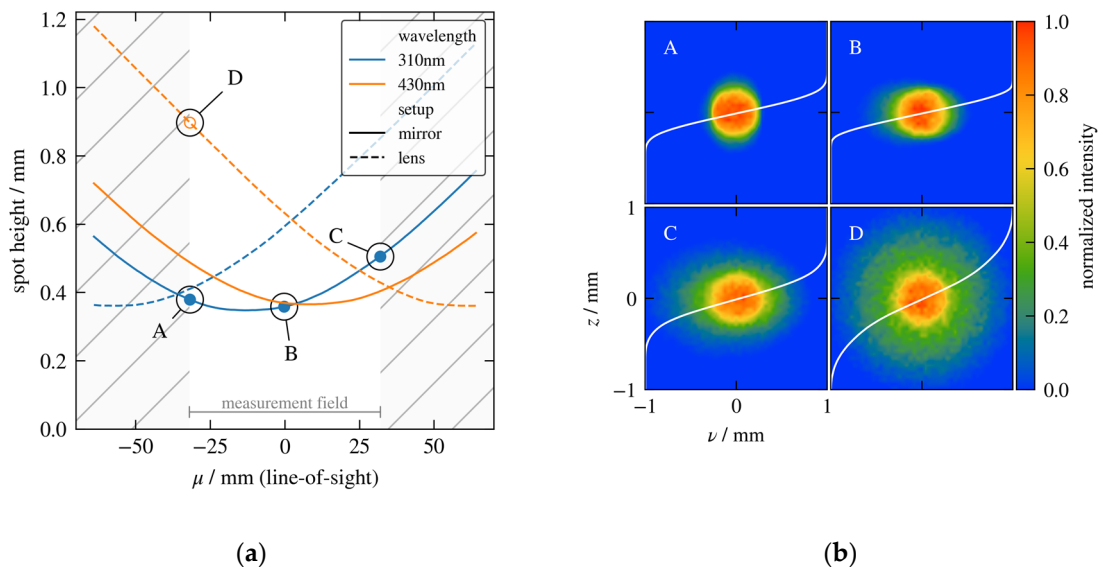
Figure 4. (**a**) Variation of the out-of-plane resolution (spot height) over the measurement field (line-of-sight direction) at 310 and 430 nm for a telescope with two lenses (dashed lines) or with a lens and tilted spherical concave mirror (solid lines). (**b**) Intensity distributions of the imaged spots and normal to the line-of-sight direction at selected positions A, B, C, and D. The white lines are cumulative probability density curves along the z-axis. See the text for the definition of the coordinate systems.

Figure 4a confirms the influence of chromatic aberrations in the purely lens-based telescope design (dashed lines). The distance in the line-of-sight direction between the focal planes (minima) at 310 and 430 nm was about 120 mm. Thus, the vertical extent of the imaged volume would change at both wavelengths by more than a factor of two. In the new telescope design (solid lines), however, the curves of both wavelengths were much closer to each other and the variation of the vertical resolution over the measurement area is only about 25%. The same applied to the horizontal resolution, but spherical distortion and the tilted curved mirror caused an asymmetry, whereby the positions of the minimum spot sizes in the vertical and horizontal directions did not coincide. In this work, the distance between the telescope and the measurement area was set to optimize the out-of-plane resolution. The in-plane resolution was mainly determined by the distance between the cells in the reconstruction grid (see below).

Towards the camera, the optical fibers were brought together in a single ferrule in which the individual fiber rows were stacked one above the other, each separated by a 765 µm stainless steel spacer (Figure 5). The output signal of the optical fibers was collimated by an off-axis parabolic mirror (OPM1, UV-enhanced aluminum, ø2 inch, reflected focal length 152.4 mm) and deflected by a flat elliptical mirror (EM1) through a short-pass filter (SP, cut-off wavelength: 450 nm, ø2 inch) and a wedged prism (WP, quartz, anti-reflection coated, ø2 inch, prism angle: 9°). The signal of each individual optical fiber was spatially separated into its wavelengths by the prism and imaged through another set of mirrors (EM2 and OPM2) onto the ICCD camera. The prism was oriented so that the spatial separation of the signal on the camera sensor as a function of the wavelength was perpendicular

to the fiber rows. A band-pass filter (BP) could be inserted to limit the detection to the emission wavelength of a single species.
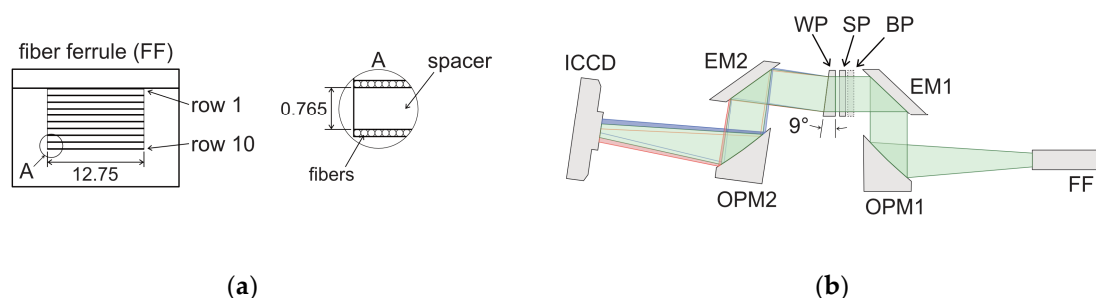
Figure 5. (**a**) Arrangement of stacked fiber rows; (**b**) optical layout of the relay optic between the fiber output and the image intensified charged coupled device (ICCD) camera. The signal of each individual optical fiber was spatially separated into its wavelengths by a prism and imaged onto the camera. (FF: fiber ferrule, OPM: off-axis parabolic mirror, EM: flat-elliptical mirror, BP: band-pass filter (optional), SP: short-pass filter, WP: wedged prism).

The spacer between the rows (Figure 5a) ensures that a broad spectral range of 300 to 800 nm could be detected without appreciable superposition or cross-talk of the signals of neighboring fiber rows. While the short-pass filter blocked all transmissions between 450 and 720 nm, it allowed light at even longer wavelengths to pass through again (Figure 6a). At the same time, the quantum efficiency of the image intensifier of the CCD camera at wavelengths greater than 700 nm was less than 1% and essentially zero above 800 nm. This combination ensured first that effectively no light with wavelengths larger than 800 nm was detected, thus avoiding crosstalk of the signals of adjacent rows due to spectral dispersion. Secondly, the emission of a sooting flame at wavelengths larger than 720 nm was intense enough to compensate for the low quantum efficiency of the photocathode. Therefore, soot signals between 720 and 800 nm could be detected, well separated from the emissions at 310 nm (OH*) and 430 nm (CH*). For comparison, Figure 6a also shows the black body spectrum at a soot temperature of 2000 K. At 750 nm the soot radiation was already about four orders-of-magnitude more intense than at 310 nm. As a consequence, we did not observe any soot radiation at 310 nm (OH*) but soot emissions at 430 nm were still intense enough to contaminate the CH* emission and soot may spectrally overlap in sooting flames.

As an example, Figure 6b shows the signal of a laminar methane/air diffusion flame at different heights above the burner (see also Section 3.2). The inset is a small section of a single fiber row, which has been spectrally dispersed by the prism, while the solid and dashed lines in the main figure are the normalized optical spectra of the highlighted optical fiber at different heights above the burner. For the spectrum, all pixel intensities within the white dashed rectangle have been binned together perpendicular to the indicated wavelength axis. At $h = 5$ mm the flame emission is almost solely caused by OH* and CH*, while at $h = 15$ mm soot emission starts to emerge with a maximum at 750 nm. The bottom *x*-axis is the pixel position relative to the OH* emission at 310 nm. Based on the wavelength-dependent refractive index of the wedged fused silica prism and the distance between the prism and the camera sensor, the pixel position is linked to the wavelength (top *x*-axis). The assignment was confirmed by measurements with narrowband bandpass filters at 310, 450 and 750 nm. Since the derivative of the refractive index of fused silica sharply decreased with increasing wavelength in the measured wavelength range [63], the optical resolution in the soot emission region was significantly lower than that for OH* and CH*. Since soot has a broad emission spectrum anyway and the spectral region around 750 nm is limited by the combination of short-pass filter and quantum efficiency of the ICCD, the results and conclusions of the current work were not affected by the deteriorating optical resolution. However, the optical resolution can be adjusted or optimized for different spectral regions by selecting a different prism material and wedge angle.

(a)

(b)
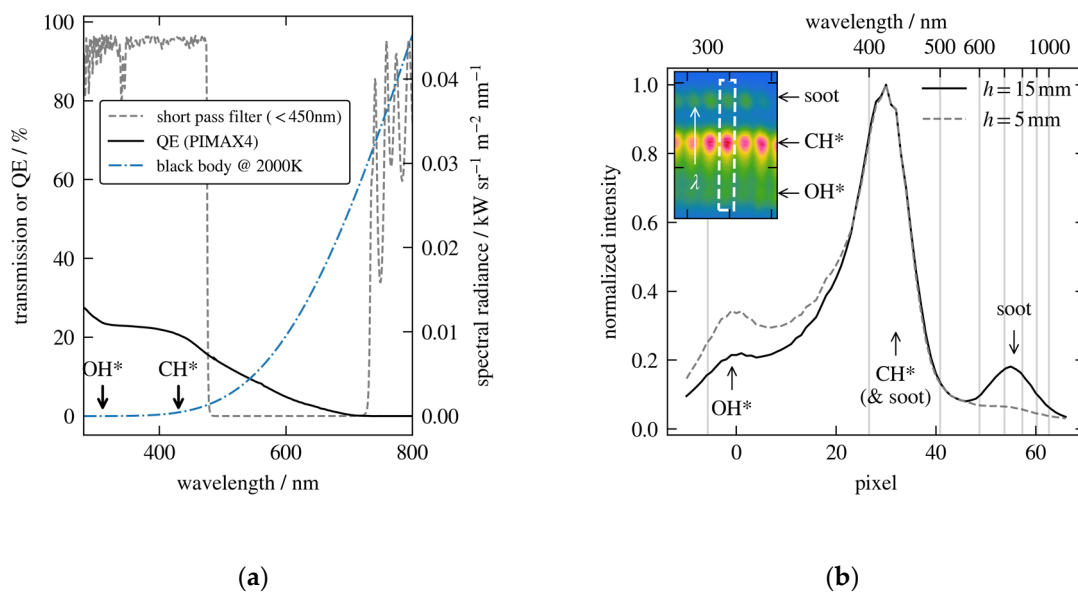
Figure 6. (**a**) Transmission curve of the short pass filter and quantum efficiency (QE) of the ICCD camera. Also shown is the black body emission spectrum at a temperature of 2000 K. (**b**) Spectral separation of the signal of a fiber row by the installation of the wedge prism for a laminar methane/air diffusion flame at different heights above the burner. The inset shows a small region of the raw camera image and the direction of increasing wavelength. Normalized spectral curves corresponding to the fiber marked by the white dashed rectangle.

Each pixel of the camera was linked to the wavelength and to its associated optical fiber, and thus the projection angle and position, by placing a point light source in the measuring plane and moving it along the fiber row of each telescope. The "point light" source consisted of a small bearing-ball (ø600 μm) attached to the tip of a thin needle, which was illuminated by a fiber-coupled xenon arc lamp or a mercury-vapor lamp. A set of band-pass filters allowed the selection of appropriate illumination wavelengths. Since the diameter of the bearing-ball was comparable to the optical resolution (see Figure 4 and Section 3.1), it illuminated at most two or three optical fibers at each position in the measurement field simultaneously. By moving the point source systematically over the field of view of each telescope, one can unambiguously assign the camera pixels to the individual fibers and account for a possibly erroneous ordering or alignment of the fibers in each fiber row. In fact, in each row, a few adjacent fibers were reversed in their order by the manufacturer, contrary to our original specifications. Thus, if the ordering or spatial assignment of the optical fibers in a fiber bundle was essential to the experiment, a detailed examination of the fiber arrangement was mandatory.

Intensity calibration factors for each individual fiber were obtained by imaging a uniformly illuminated diffusor in the center of the measuring field and by dividing the calibration signal of a single fiber by the average signal intensity of all fibers. The calibration was performed for each wavelength separately and ensured that, for a given wavelength, the detected signal of all fibers was on the same scale.

2.3. Tomographic Reconstruction

For the reconstruction, the measurement area was divided into a Cartesian grid with $n = 102 \times 102$ elements and an edge length of 64 mm. In the following, we assumed that the flame was a low scattering optical medium with homogeneous refractive index even for sooting flames, so that the light followed a straight line from the emission source in the flame to the detector. That is, index gradients

caused by fluctuations of the local flame temperature and species concentrations were neglected. Under this assumption, each projection b_i can be approximated as a "ray-sum" [21,64,65]:

$$b_i = \sum_j^n A_{ij} x_j. \tag{1}$$

Here, x_j is the unknown species concentration at pixel j and A_{ij} is the contribution of pixel j to the projection i. Reconstructing the species distribution from the set of $m = 10 \times 102$ projections then requires solving a set of linear equations,

$$Ax = b \tag{2}$$

where $b \in \mathbb{R}^m$ is a vector containing the measured projection intensities and $x \in \mathbb{R}^n$ are the unknown species concentrations. Since we are in the limit of low optical density and low optical scattering, the projection matrix $A \in \mathbb{R}^{m \times n}$ is constant, specific to the selected arrangement and only needs to be determined once (see below). However, one cannot solve for the species concentrations directly because the linear system is not well-posed, as defined by Hadamard [66]. More specifically, Equation (2) is rank-deficient meaning that it permits an infinite number of solutions and additional assumptions have to be made to limit the solution space [64,67]. Additionally, the solution does not depend continuously on the measured projections. Small changes (errors) of the projection data caused, e.g., by noise, are amplified and lead to extreme changes in the solution vector x. Both problems can be mitigated by regularization methods [64,65,67,68]. In this work, we used a combination [69,70] of 1st order Tikhonov regularization [68] and compressive sensing [71]. The species concentration was then obtained by solving the optimization problem:

$$x = \operatorname{argmin}[f(x)] \text{ with } f(x) = \|Ax - b\|_2^2 + \lambda_1 \|Lx\|_2^2 + \lambda_2 \|x\|_1^2 \text{ s.t. } x \geq 0 \tag{3}$$

and $\|\dots\|_q := \left(\sum_j |x_j|^q \right)^{1/q}$ and $L_{ij} = \begin{cases} 1 & i = j \\ -1/n_i & i \text{ neighboring } j. \\ 0 & \text{otherwise} \end{cases}$

Here $\|\dots\|_q$ denotes the Euclidian norm ($q = 2$) or Manhatten norm ($q = 1$). n_i is the number of direct neighbors to pixel i, apart from the edges of the reconstruction grid, $n_i = 4$. The Laplacian L adds an additional set of n equations to the linear system to remedy the rank-deficiency and enforces a piecewise smooth distribution. The extra term, $\lambda_2 \|x\|_1^2$, has its origin in compressed sensing theory and minimizes the number of non-zero pixels [71]. Practically, it enforces the species concentrations to be zero in areas where the signal is close to or below the noise level. In statistics, Tikhonov regularization and compressive sensing are also known as ridge and lasso regression, respectively. Since the classical L-curve method is not recommended for determining the optimal regularization parameters for the specified regularization scheme used here [64,72], the optimal parameters were determined by trial-and-error and phantom studies. Equation (3) was solved by a steepest descent solver until the scalar objective function values of two successive iteration steps fulfill the convergence criterion:

$$\epsilon_1 = \frac{f^{(p)} - f^{(p-1)}}{\max\left(f^{(p)}, f^{(p-1)} \right)} < 10^{-6} \tag{4}$$

where $f^{(p)} = f\left(x^{(p)} \right)$ is the objective function value in the p-th iteration.
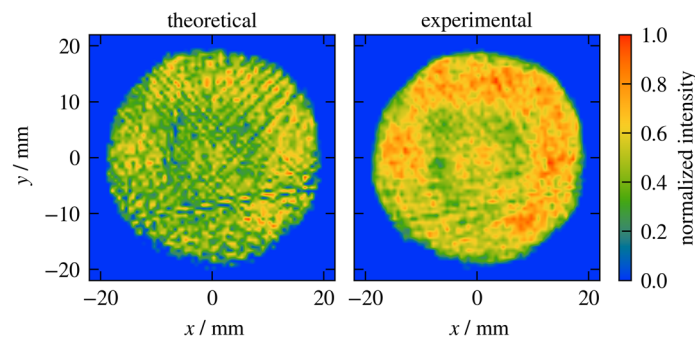
2.4. Projection Matrix

Generally, if the exact ordering and position of optical fibers, as well as the arrangement of the optical elements in the telescopes, are exactly known, one could determine the elements of the projection matrix theoretically using ray optics [21]. In practice, however, there is always a slight variation in the spacing between fibers and the position normal to the row. In addition, adjacent fibers

are not perfectly parallel to each other, especially when removing the outer cladding to accommodate more optical fibers in each row. In 3D-tomography one could simply use a suitable optical target to obtain the projection matrix and to assign the voxels to the line-of-sights of each camera pixel [30]. Here we used the same arrangement with the point light source as in the previous section for assigning the camera pixels to the optical fibers, but now the point light source was scanned over the full reconstruction grid. At each grid point j, the intensity I_{ij} was measured for each fiber i, with at most three fibers having any measurable intensity for each telescope and grid point. The projection matrix was then normalized by dividing the measured intensity by the total intensity of the respective fiber:

$$A_{ij} = I_{ij} / \left(\sum_{k=1}^{n} I_{ik} \right).$$

(5)

The projection matrix was determined individually for each wavelength to compensate for chromatic aberrations.

Figure 7 shows a comparison between theoretically and experimentally determined projection matrices using a premixed flat laminar methane-air flame [21] as an example. The theoretical projection matrix was developed based on the geometric arrangement and properties of the optical components using our in-house ray-tracing algorithm [62], which is similar to the method in Reference [21]. Using the theoretical projection matrix, reconstruction artifacts can be clearly identified, which express themselves primarily in linear streak-like structures. They are due to deviations between the nominal position and alignment of the individual optical fibers compared to the actual values. In the reconstruction based on the experimentally determined projection matrix, the artifacts were much less pronounced or disappeared. All species distributions shown in the remainder of the manuscript were calculated using the experimental projection matrix, although the artifacts were much less pronounced for the annular diffusion flames discussed below.


Figure 7. Reconstruction of a round premixed flat methane/air flame using either a theoretically (left) or an experimentally (right) determined projection matrix. (310 nm, exposure time 60 ms, $\lambda_1 = 5$, $\lambda_2 = 10$, $\phi = 1.0$, $V = 12$ slm).

3. Results

3.1. Spatial Resolution

Figure 8 shows a typical reconstruction of the OH* distribution at 310 nm obtained from a laminar methane/air diffusion flame 1 mm above the nozzle exit. In contrast to the previous work [20], we were able to avoid a lift-off of the flame by suitable starting conditions (very low initial flow of methane that was slowly increased to its operational value), so that the flame was almost perfectly circular and fluctuated only slightly at the nozzle exit. The single shot image was taken at an exposure time of 100 ms and the reconstruction was done with the regularization parameters set to $\lambda_1 = 5$ and $\lambda_2 = 10$. The compressive-sensing term in Equation (3) effectively eliminated artificial intensities at the flame edge and in the center of the flame. At the same time, the contribution of the Tikhonov term was chosen so that the reconstructed flame front is not measurably broadened. Figure 8 also shows a

magnification of the flame front, superimposed with the numerical reconstruction grid. A single grid cell was 0.63×0.63 mm^2 in size and the flame front was mapped by about two to three grid cells with high intensity. Since the flame front was much thinner than 1 mm, this resulted in an effective optical resolution in the tomographic measurement plane of about 2 cells or ~ 1.3 mm, in accordance with the Nyquist-Shannon sampling theorem.
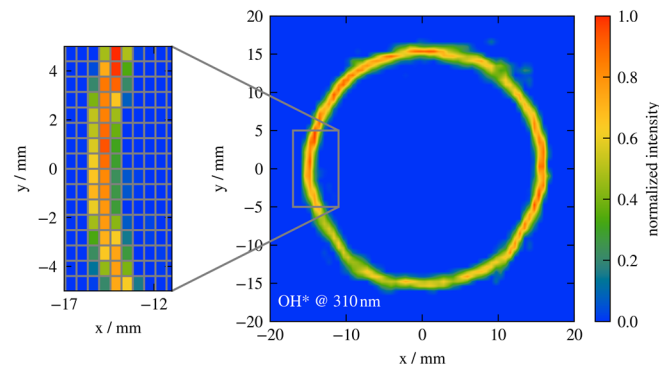
Figure 8. Typical reconstruction of a laminar methane/air diffusion flame obtained 1 mm above the nozzle exit (OH* @ 310 nm, exposure time 100 ms, $\lambda_1 = 5$, $\lambda_2 = 10$, CH$_4$ 2.0 slm, air 10.0 slm). The inset is a magnification of the flame front superimposed with the numerical reconstruction grid (grid cell size 0.63×0.63 mm^2).

The quality of alignment of the telescopes was experimentally tested by measuring the chemiluminescence signal of OH* (310 nm) and CH* (430 nm) of a premixed flat flame as a function of the vertical position of the burner matrix as described by Anikin et al. [21]. For each optical fiber intensity profiles were measured at several heights z above the burner. These profiles, normalized to their respective maximum value, are shown in Figure 9a. The solid line represents the average signal intensity profile obtained for all fibers and both wavelengths, while the gray dashed line is the profile of a single fiber. The shaded area is the 1σ-interval of the average profile. Considering that the thickness of the flame front (<200 μm) is much smaller than the width of the profile, the optical resolution perpendicular to the measurement plane approximately equals the full-width-at-half-height (FWHM) of the averaged profile, which is 0.9 ± 0.3 mm. This value is very close to that given in the previous section for the in-plane resolution. Finally, Figure 9b shows the distribution of the position of the maximum intensity (z_{max}) of all individual fiber profiles, separated by wavelengths. There is a small shift of a few tens of microns between the distributions at 310 nm and 430 nm. However, for both wavelengths 80% of fibers have their maximum signal intensity within 350 μm, which is only slightly larger than that obtained in our previous work for the single wavelength POET [21]. Thus, all projections are aligned in the same plane with an accuracy that is significantly below the optical resolution.

In general, the desired optical resolution, defined by the magnification factor and the $f_\#$-number (or numerical aperture) of the telescopes, must be weighed against the intensity of the signal to be measured or the sensitivity of the detector. The imaging optics and optical resolution chosen here represent a compromise in which the distributions of chemiluminescent species in turbulent flames can be reconstructed with high reliability at an exposure time of 1 ms, corresponding to a repetition rate of 1 kHz.

(**a**)   (**b**)
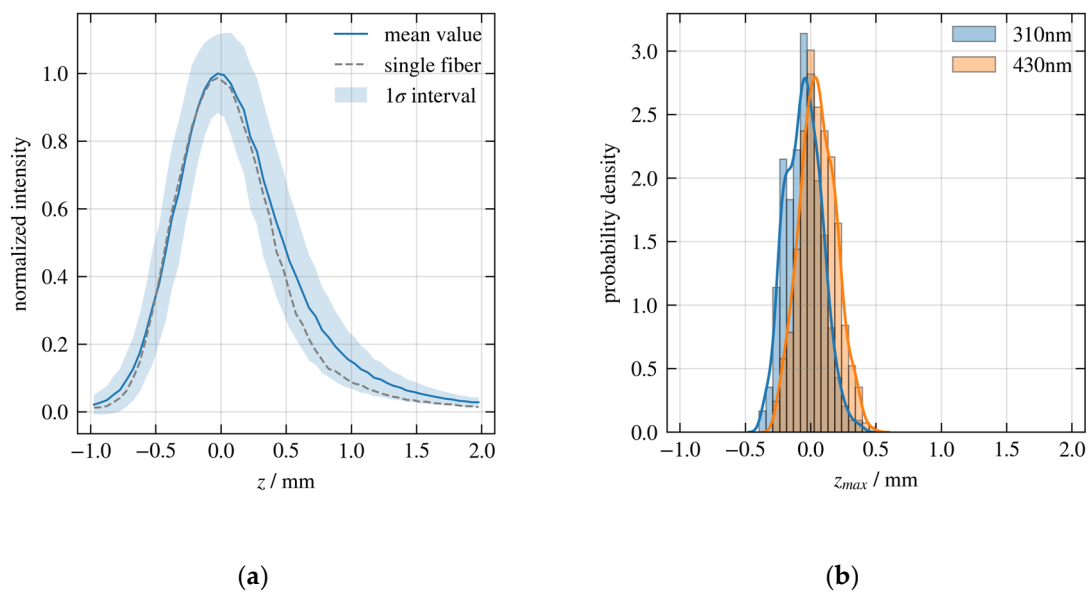
Figure 9. (**a**) Average intensity profile obtained by scanning a premixed flat laminar flame vertically through the measurement plane. The z-axis is normal to both, the flat flame and the tomographic plane and the flame front is at $z = 0$ mm. (**b**) Distributions of the position of the maximum intensity of each individual optical fiber, separated by wavelength.

3.2. Simultaneous Multi-Wavelength Detection

One of the key innovations of the new tomographic setup is the ability to detect multiple wavelengths and thus different species simultaneously. We will first demonstrate the capabilities of multi-wavelength detection on a laminar methane-air diffusion flame. A typical image of a reconstructed intensity distribution at 310 nm and just above the burner opening has already been shown in Figure 8 (see also Video S1). The distribution at 430 nm looks almost identical. The coordinates x and y are in the tomographic measurement plane, which is oriented parallel to the exit plane of the burner. The z-axis coincides with the vertical burner axis, with $z = 0$ mm at the burner exit (see Figures 1 and 2). Figure 10 shows time-averaged intensity distributions at 310, 430 and 750 nm in a vertical plane at $y = 0$ mm. For the vertical sections, images were taken at different heights above the burner. The step size in the z direction was $\Delta z = 0.3$ mm. At each position, the reconstructed distributions were averaged over 300 images witch an exposure time of 100 ms each. The apparent broadening of the flame front above $z > 10$ mm is due to the fluctuation of the flame. In the lower part, however, the flame is stationary.
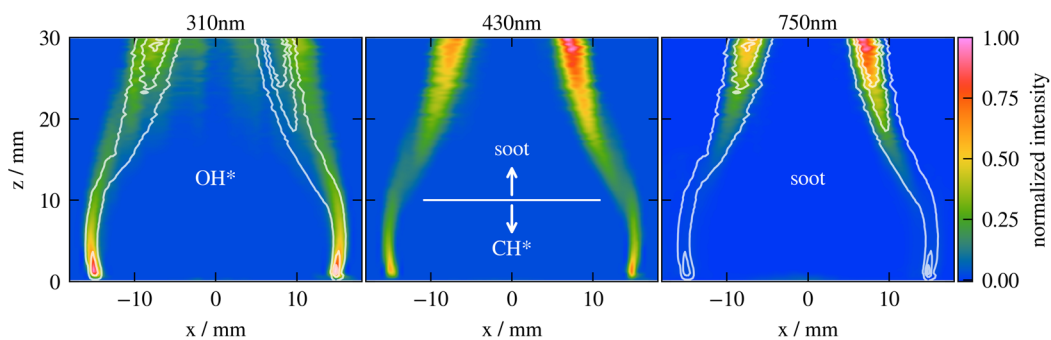
Figure 10. Vertical slices ($y = 0$ mm) of the time-averaged intensity distributions of a laminar methane/air diffusion flame at 310, 430 and 750 nm ($\lambda_1 = 5$, $\lambda_2 = 10$, CH_4 2 slm, air 10 slm). The white solid lines are 10%, 40% and 60% iso-contour lines of the distribution at 430 nm.

At 750 nm we only detected the thermal radiation of soot particles, whereas at 310 nm the thermal soot emission was already lower by four orders of magnitude, so that just OH* contributed to the emission signal. In contrast, the soot emission at 430 nm was still intense enough to superimpose the CH* emission. This is exactly what can be observed in the vertical sections in Figure 10 and is illustrated by the iso-contour lines at 430 nm (white solid lines). Directly above the burner exit, there is no soot and the emission at 430 nm stems solely from CH*, which is spatially very well correlated with that of OH* (see left figure). Above $z = 10$ mm, soot particles start to appear. Simultaneously, the emission at 430 nm moves inward, into the area of the unburnt fuel, and spatially overlaps with the soot emission. Therefore, the interpretation of the emission at 430 nm must always take into account the possibility of overlapping with the thermal radiation of soot particles. In the case of the laminar diffusion flame shown here, however, the assignment is straight forward.

Pure fuel was in the center of the flame and outside, with increasing radial distances to the center, ambient air. Between these two regions was the reaction zone in the vicinity of stoichiometric mixture conditions. Due to the strong temperature increase towards the flame front, the fuel was pyrolyzed between the reaction zone and the center, and soot particles were formed. Thus, as expected, the soot formation zone (750 nm) was closer to the center of the flame (the pure fuel) than the reaction zone of the flame front. The latter was clearly characterized by the OH* emission (310 nm). This is also evident in Figure 11 where horizontal cross-sections (left) and slices in the radial direction (right) through the flame are shown at two different heights above the burner. At $h = 5$ mm, there was no signal at 750 nm (soot) and the signals at 310 nm (OH*) and 430 nm (CH*) spatially overlapped, whereas at $h = 15$ mm, the signals at 430 and 750 nm (now both are soot) overlap and were closer to the center than the signal at 310 nm (still OH*). Finally, it was obvious that the soot particles were completely oxidized by approaching the reaction zone of the flame. As a consequence, we were very likely detecting the flame structure correctly and it was not dominated by reconstruction artifacts.


(**a**)　　　　　　　　　　　　　　　　　　　　　　(**b**)
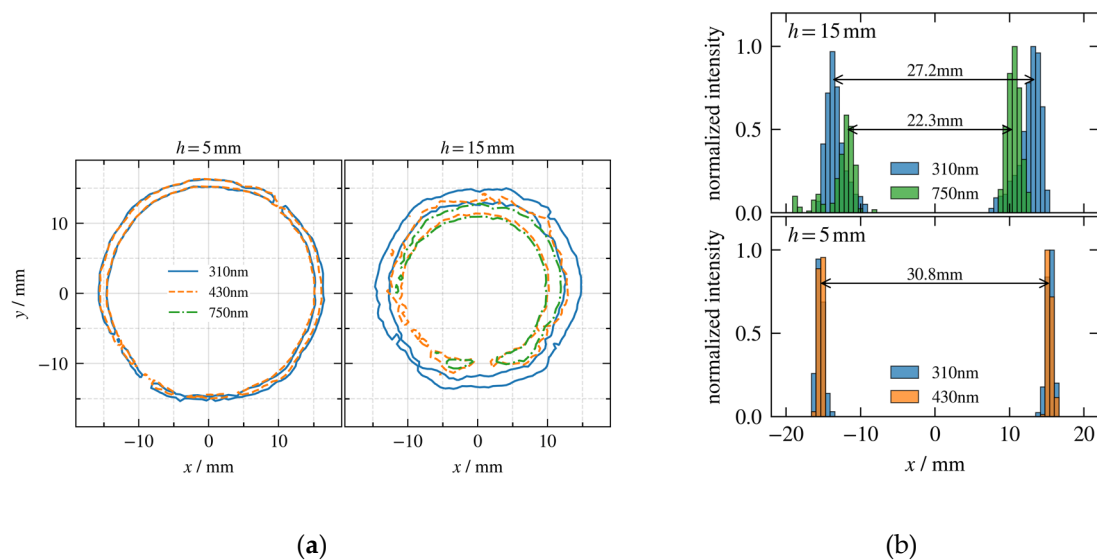
Figure 11. (**a**) Iso-lines of horizontal cross-sections at $h = 5$, and $h = 15$ mm. (**b**) 1D radial profiles through the center of the horizontal slices.

3.3. Application to Turbulent Flames

In the previous sections, we validated the alignment of the telescopes and showed that the tomographic setup was indeed capable of imaging OH* (310 nm), CH* (430 nm) and soot (750 nm) simultaneously. Additionally, it was shown that the respective spatial species distributions can successfully be reconstructed. In the following, we present the results obtained in turbulent flames. Figure 12 shows typical, simultaneously measured distributions of OH* (left) and CH* (right) of a non-sooting turbulent methane-air diffusion flame obtained 13.3 mm above the burner, at an exposure

time of 1 ms (see also Video S2). In addition, the color-coded distributions were superimposed with the 25% isolines of the other wavelengths/species, respectively. The electronically excited species OH* and CH* are commonly used as flame front markers because their spatial location is inherently tied to the position of maximum heat release rate, even in turbulent flames [11]. This position also changes only slightly with the strain rate and curvature of the flame front [11]. The same applies to the ratio of the chemiluminescence intensities, at least under moderately turbulent conditions [2,9,11].
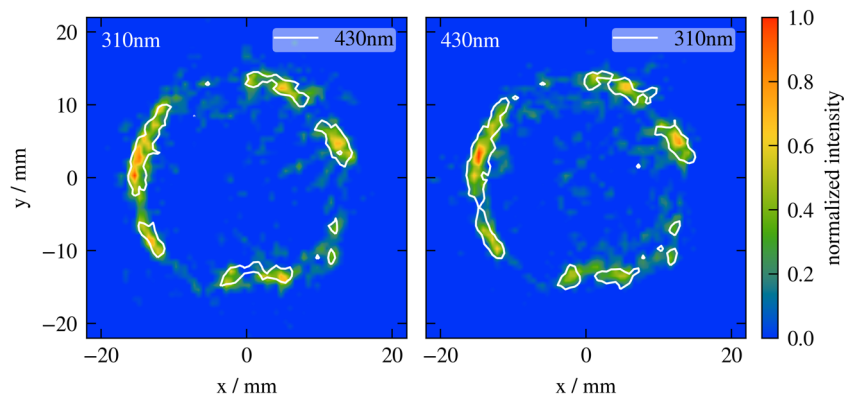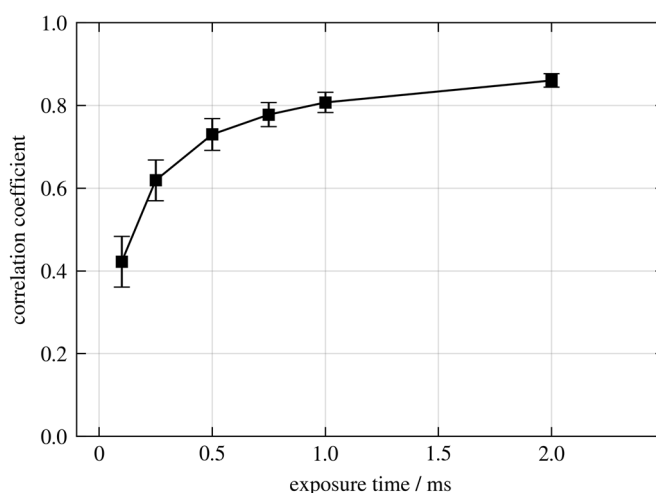

Figure 12. Simultaneously acquired, normalized species distributions of OH* (310 nm, left) and CH* (430 nm, right) measured in a non-sooting turbulent methane/air diffusion flame at $h = 13.3$ mm above the burner with an exposure time of 1 ms ($\lambda_1 = 5$, $\lambda_2 = 5$, CH$_4$ 2 slm, air 100 slm). The white solid lines are the 25% isolines of the other wavelengths/species, respectively.

As expected, and within the optical resolution of the tomographic setup, we observed a very good spatial overlap of the measured OH* and CH* distributions within each individual exposure. This can be quantified by calculating the normalized correlation coefficient [73] of the two distributions:

$$\rho(\boldsymbol{x}, \boldsymbol{y}) = \frac{\sum_i (x_i - \overline{x})(y_i - \overline{y})}{s_x s_y} \quad i = 1 \ldots n \tag{6}$$

where $\overline{x}$ and $\overline{y}$ are the mean values and s_x and s_y the standard deviations of the two distributions $\boldsymbol{x}$ (OH*) and $\boldsymbol{y}$ (CH*). The correlation coefficient captures the most important contribution to the structural similarity index (SSIM) [74] that was recently used by Liu et al. in a phantom study [33]. $\rho(\boldsymbol{x}, \boldsymbol{y})$ and SSIM are practically identical over the entire range of exposure times and within the standard deviation. The result is shown in Figure 13 as a function of the exposure time in the range of 0.1 to 2.0 ms. Each point is the average correlation coefficient of a series of at least 500 simultaneously acquired distributions and the error bars reflect the 1σ-standard deviations. At an exposure time of 1 ms the correlation coefficient was ~ 0.8, indicating that the OH* and CH* distributions were very similar. This means that we were very likely to correctly detect the flame structure and that it was not dominated by reconstruction artifacts. The remaining uncertainty was due to reconstruction artifacts caused by measurement noise. If the exposure time was successively reduced, the signal became weaker and weaker until the noise became dominant. Since the noise fluctuations for both species were statistically independent of each other, the correlation disappeared at low exposure times or low signal-to-noise ratios.
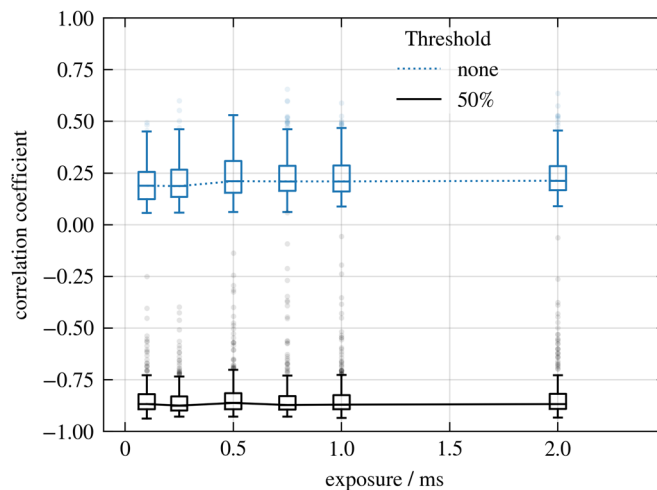
Figure 13. Normalized cross-correlation between simultaneously acquired distributions of OH* and CH* in a turbulent methane/air diffusion flame (compare Figure 12) as a function of image exposure time.

Figure 14 shows reconstructed instantaneous species distributions of a sooting turbulent ethylene/air diffusion flame at three wavelengths: 310 nm, 430 nm, and 750 nm (see also Video S3). At 310 nm and 750 nm only OH* and soot, respectively, contribute to the signal, while both CH* and soot give rise to the signal at 430 nm. As discussed above in the context of sooting laminar diffusion flames, the results obtained in turbulent flames confirm the assignment. As expected, the OH* and CH* distributions overlap spatially and strong OH* (or CH*) and soot signals are mutually exclusive [75,76]. The latter is expressed quantitatively by the normalized correlation coefficients in Figure 15. If we limit the correlation to the most intense features in both distributions (>50% of the maximum value), the correlation coefficients are strongly negative (black line) and, as previously mentioned, the occurrence of the associated features is mutually exclusive. Such behavior is consistent with the fact that soot particles form on the side of the flame facing the fuel, in other words, their occurrence is spatially displaced from the reaction zone. The blue line corresponds to the mean correlation coefficients between the distributions of OH* and soot for all pixels, that is without any filtering. Over the entire measuring field, both soot and OH* are more or less weakly correlated with each other, since soot particles are formed in the vicinity of the flame front and partially overlap with each other. Both correlations are also independent of the exposure time, as they should be.
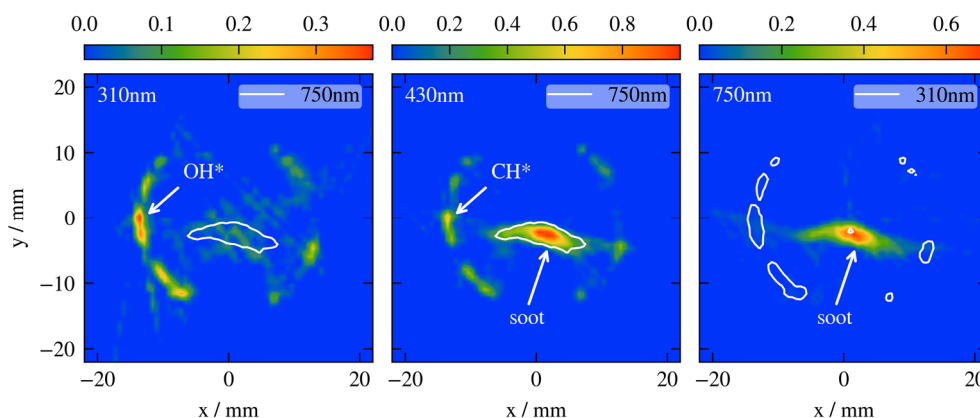

Figure 14. Simultaneously acquired, normalized distributions at 310 nm (OH*, left), 430 nm (CH* + soot, middle) and 750 nm (soot, right) measured at a turbulent ethylene/air diffusion flame 4 mm above the burner with an exposure time of 1 ms ($\lambda_1 = 5$, $\lambda_2 = 5$, C_2H_4 2 slm, air 100 slm). The white solid lines are the 25% isolines of distributions at 750 nm (left and middle) or 310 nm (right).

Figure 15. Normalized correlation coefficients between the OH* and soot distributions in a turbulent ethylene/air diffusion flame (compare Figure 14) without filtering (blue, dotted) and by limiting the correlation to the most intense features (black, solid).

Finally, Figure 16 shows 3D images of time-averaged intensity distributions of OH* or OH* and soot in (a) the non-sooting turbulent methane/air and (b) sooting turbulent ethylene/air diffusion flames, respectively. Experimentally, the measurement plane of the tomographic setup was slowly scanned from the burner exit downstream through the flame. At each point, an image of the flame was taken with an exposure time of 100 ms and the frames were later assembled into a 3D distribution. The general structure is the same as that in the instantaneous 2D distributions (Figures 12 and 14).

(a)

(b)
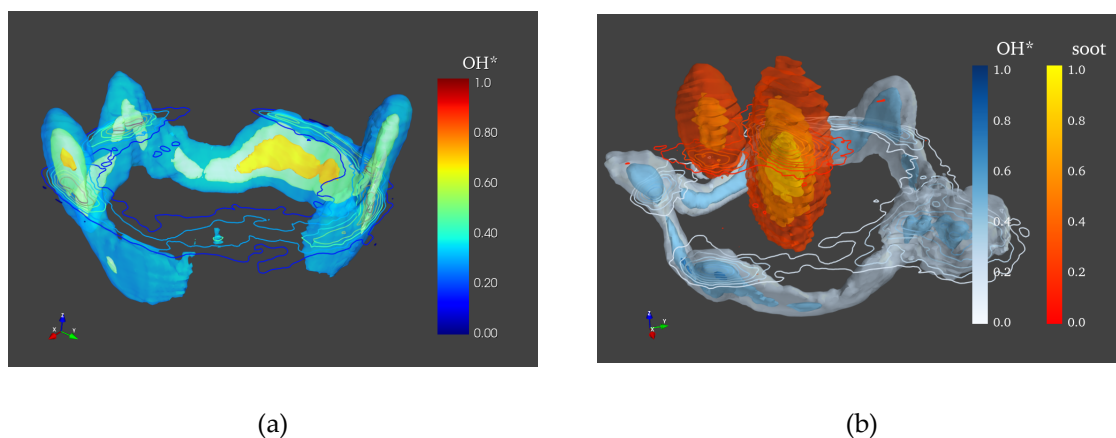
Figure 16. Time averaged 3D distribution of (**a**) OH* in a non-sooting turbulent methane/air diffusion flame (compare Figure 12) and (**b**) of OH* and soot in a sooting turbulent ethylene/air diffusion flame (compare Figure 14).

4. Discussion

It is well known that the local equivalence ratio in premixed flames correlates with the ratio of the intensities of OH* and CH* [2,4,6,8–13,77]. This relationship can be used to monitor the flame stoichiometry online. For example, Orain and Hardalupas [13] demonstrated local, time-dependent measurements of the fuel-to-air ratio in a swirl stabilized, nominally non-premixed burner. Using the intensity of chemiluminescence from OH* and CH* they could differentiate between regions of non-premixed, lean, stoichiometric and rich combustion and showed that combustion occurred in a partially premixed mode for all flow conditions, although fuel and air were injected separately in the reaction zone. The majority of the investigations to date have been time-resolved single point measurements using a Cassegrain optic in laminar [2,6] and turbulent flames [8,9,13]. Radial profiles

were obtained by scanning the probe volume through the flame. Here, multi-species tomography offers the possibility of spatially (and potentially temporally) resolved measurements of the local fuel-to-air ratio.

This approach was first tested on premixed flat methane/air flames (compare Figure 7 and Reference [21] for the burner setup) with different equivalence ratios. The corresponding median intensity ratio I_{OH*}/I_{CH*} as a function of the equivalence ratio is shown in Figure 17a (open circles). Each point represents the median over all pixels in the reconstructed images. Here we use the median of the distribution instead of the mean because it is a more robust statistical measure for the highly skewed distributions (see below). Pixels with an intensity of less than 10% of the maximum intensity in each image have been omitted. The 1σ-standard deviation is $\pm 0.35\ldots 0.4$. The median ratio of the radon projections of both species (gray solid line) is also shown. For the calculation, the radon projections of all optical fibers in each image and for each species were summed up before taking the intensity ratio. This is justified because for a premixed, flat flame, the local equivalence ratio is identical at every point on the flame front. Hence, the intensity ratio of the radon projections is a measure of the true intensity ratio at the given equivalence ratio. In contrast, the intensity ratio in the reconstructed distributions has been calculated individually at each pixel in every image.

(**a**)   (**b**)
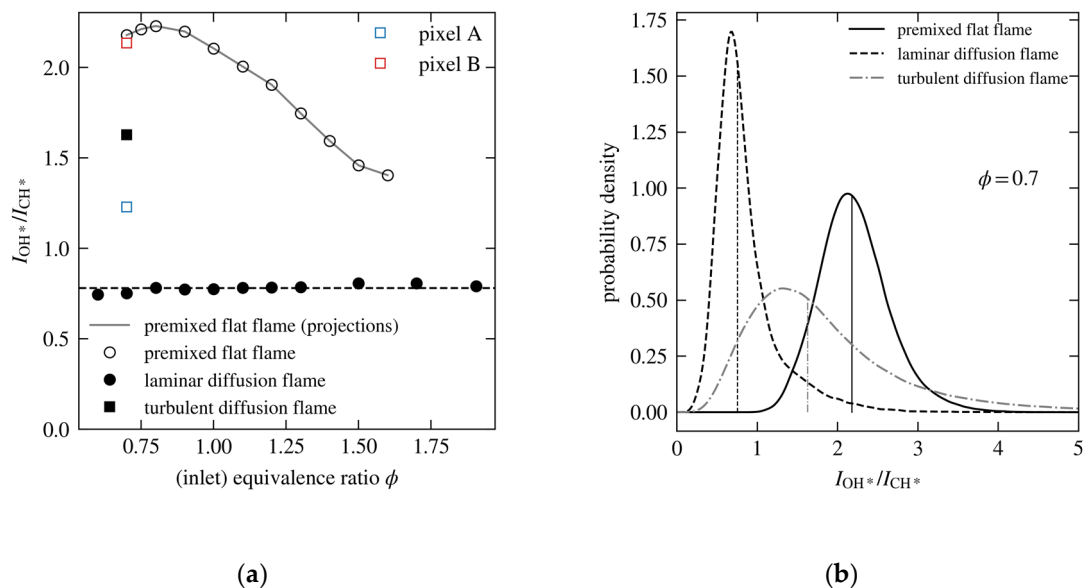
Figure 17. Evaluation of the intensity ratio I_{OH*}/I_{CH*} for a premixed flat flame as well as laminar and turbulent diffusion flames (all methane/air): (**a**) Median intensity ratio as a function of (global) equivalence ratio. The gray solid line is the intensity ratio of the premixed flame obtained directly from the radon projections. Open squares represent median values of the turbulent flame for selected individual pixels (see text for more details). (**b**) Intensity ratio distribution at $\phi = 0.7$ evaluated over all pixels of the reconstructed distributions. Vertical lines indicate the median intensity ratio. For diffusion flames, the equivalency ratio refers to the fuel-air ratio between the separate input streams of methane and air.

Overall, the dependency of the intensity ratio I_{OH*}/I_{CH*} of the premixed flame corresponds qualitatively with literature data: the intensity ratio decreases with increasing equivalence ratio. Intensity ratios derived independently from the radon projections (solid line) and the reconstructed images (open circles) are identical, confirming that it is indeed possible to reliably derive mean intensity ratios from tomographic measurements. The exact shape of the curve depends crucially on the experimental setup and spectral analysis [77]. Additionally, quantitative deviations are to be expected since the optical sensitivity of the detection system has not been calibrated at both wavelengths.

However, the results discussed below remain unaffected, since the calibration will only change the absolute value of the intensity ratio, but not the shape of the curve on the equivalence ratio.

Figure 17a also contains intensity ratios obtained from laminar and turbulent methane/air diffusion flames. For both diffusion flames, the given equivalence ratio represents the fuel-air ratio between the separate inlet flows for methane and air. As expected, the intensity ratio and, thus, the fuel-to-air ratio in the flame front of a laminar diffusion flame (filled circles, $h = 5$ mm, compare Figures 10 and 11) is constant and independent of the global equivalence ratio. The flame always burns at the same fuel-to-air ratio. The horizontal dashed line indicates the mean intensity ratio of the laminar diffusion flame. Consistent with literature data, the intensity ratio under non-premixed conditions is much lower compared to premixed combustion [11,13,27]. In contrast, the median intensity ratio of a turbulent diffusion flame (nominal inlet $\phi = 0.7$, $h = 13.3$ mm) is between that of the laminar and premixed flames, indicating that under turbulent conditions combustion is more like that of a premixed or partially premixed flame, even though fuel and air are supplied separately [13,27]. In other words, fuel and air are thoroughly mixed in the turbulent flow field.

Probability density functions (PDF) of the intensity ratio for the premixed flat as well as laminar and turbulent diffusion flames are shown in Figure 17b. All PDFs were obtained at an inlet stream equivalence ratio of $\phi = 0.7$. Vertical lines represent the locations of the median intensity ratios. Under premixed conditions, the PDF is nearly symmetric, but on an absolute scale somewhat broader compared to the laminar diffusion flame. The latter is due to small manufacturing errors in the positioning of the optical fibers perpendicular to the fiber row. Considering the imaging ratio of the telescopes ($M = 5.7$), a positioning inaccuracy of the optical fibers of 15 μm results in a vertical positioning error (out-of-plane) of the measurement volume of ~ 85.5 μm. This is already a significant fraction of the laminar flame thickness (<200 μm) and about 10% of the out-of-plane resolution. As a result, not all optical fibers might sample the flat flame at identical vertical locations, leading to a larger uncertainty in the intensity ratio. Laminar diffusion flames are only marginally affected by this inaccuracy because the flame front only slightly varies along the direction perpendicular to the measurement plane (burner axis) and within the spatial resolution. The distribution of intensity ratios of the turbulent flame is very broad, strongly right-skewed and lies between those of the laminar diffusion flame and premixed flat flame. The broadness and skewness are, to a large extent, a direct consequence of reconstruction errors and the fact that we take the ratio of two quantities with considerable noise levels. For comparison, the PDF of the mixture fraction obtained by Orain and Hardalupas [13] using single point measurements and Cassegrain optics would translate to a width of the intensity ratio distribution of only $\approx \pm 0.1$.

Local, spatially-resolved intensity ratios I_{OH*}/I_{CH*} are shown in Figure 18 for (a) a premixed, flat flame (100 ms. exposure), (b) a laminar diffusion flame (100 ms exposure, $h = 5$ mm), (c) an instantaneous image of a turbulent diffusion flame (1 ms exposure, $h = 13.3$ mm) and (d) the mean intensity ratio of the same turbulent flame (averaged over 300 images). All images were obtained at methane/air flames with an inlet stream equivalence ratio of $\phi = 0.7$. In the case of the premixed flat and laminar diffusion flame, the intensity ratio is approximately constant over the whole flame front. The diverging color scale in the image has been centered at a value of $I_{OH*}/I_{CH*} = 1.2$, thus coarsely separating non-premixed (blue) from premixed or partially-premixed (red) combustion regions.

The snapshot of the turbulent flame (Figure 18c) suggests the existence of areas with intensity ratios that are similar to those of non-premixed and premixed combustion. However, when interpreting the resulting intensity ratios, the greater uncertainties in the reconstructed absolute intensities at short exposure times (low signal-to-noise ratio) must be considered. More robust statements can be made using the averaged combustion field in Figure 18d. It shows a radial dependency of the intensity ratio, which suggests a transition from non-premixed to premixed or partially-premixed combustion with increasing distance from the burner axis. We can also analyze the PDF of single pixels or pixel regions over a series of images. This is shown in Figure 19 where we plot the PDFs for pixels with predominant non-premixed (A) or (partially) premixed (B) combustion. The PDFs in both regions are markedly

different and shifted against each other. Vertical dashed lines mark the median of the respective distribution. The median values have also been included in Figure 17a (open squares). It is evident that pixel region A is somewhere between non-premixed and premixed combustion, whereas pixel region B is very close to the intensity ratios observed in premixed combustion. Again, the distributions of intensity ratios are quite broad due to reconstruction errors and a quantitative analysis should be carried out with caution. Nevertheless, our tomographic measurements allow qualitative, but spatially resolved, statements about the mean fuel-to-air ratio or the combustion mode, which is sufficient for many industrial, diagnostic applications.
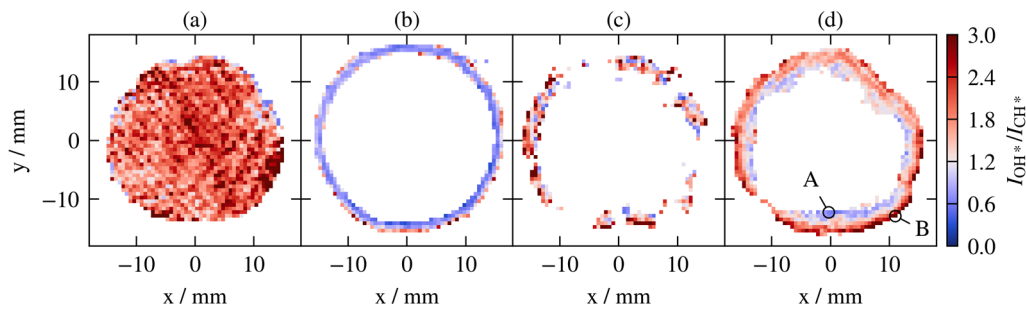

Figure 18. Local intensity ratio of OH* and CH* emission for (**a**) a premixed flat flame, (**b**) a laminar diffusion flame, (**c**) an instantaneous image of a turbulent diffusion flame at 1ms exposure time and (**d**) the time average of a turbulent diffusion flame. The inlet equivalence ratio in all cases is $\phi = 0.7$.
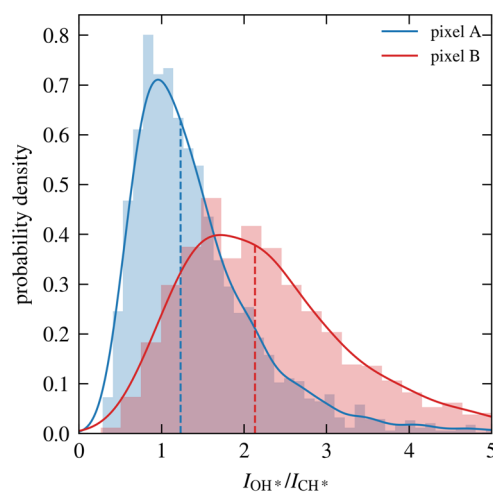
Figure 19. Probability density function (PDF) of the intensity ratio distribution of the turbulent methane/air diffusion flame in Figure 18, evaluated at pixel regions A and B.

Finally, we will consider the dependence of the intensity ratio I_{OH*}/I_{CH*} in turbulent diffusion flames on the exposure time and reconstruction algorithm. Figure 20a shows a comparison of different statistical measures (mean, median and mode) for the center of the intensity ratio distributions as a function of exposure time and using the reconstruction algorithm in Equation (3). With decreasing exposure time (or decreasing signal-to-noise ratio) the mean value increases, while the mode decreases. At the same time, the median remains almost unchanged. Both observations result from an increasing skewness of the distributions with shorter exposure times, primarily due to increasing inaccuracies in the absolute intensities of the reconstructed distributions. Under such conditions, the median is a much better descriptive statistical measure than the mean because it is less affected by extremely large or small values in a skewed distribution. As a reference, Figure 20 also shows the median intensity ratio directly obtained from the radon projections, which is independent of the exposure time. Since the

intensity ratio within the turbulent flame is not constant, unlike for the premixed flat flame (see above), the median of the radon projections is only an averaged value over the entire flame.

(**a**)   (**b**)
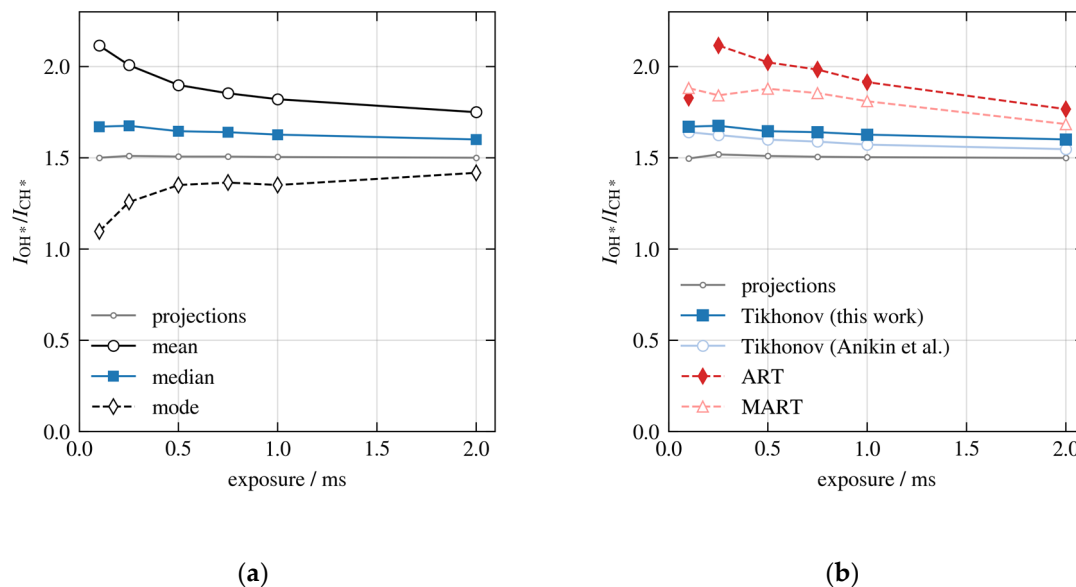
Figure 20. (**a**) Statistical measures of the intensity ratio distribution in turbulent flames as a function of exposure time and when using the reconstruction algorithm in Equation (3). (**b**) Comparison of the median intensity ratio in turbulent diffusion flames between different reconstruction algorithms. Also shown is the median intensity ratio obtained directly from the radon projections.

Overall, the median of the reconstructed distributions is a robust statistical measure to characterize the I_{OH*}/I_{CH*} intensity ratio because it is (1) very close to the intensity ratio of the radon projections and (2) almost independent of the exposure time or signal-to-noise ratio. However, this is only true for the Tikhonov regularization used, for example, in this work or by Anikin et al. [20,21], as shown in Figure 20b. The figure also contains median intensity ratios obtained when using the algebraic reconstruction technique (ART) [78,79] or multiplicative algebraic reconstruction technique (MART) [78–81]. Details on the reconstruction algorithms and an in-depth analysis of their accuracy in the limit of low signal-to-noise ratios can be found in Part II [60]. For ART and MART, the median intensity ratio increases significantly with decreasing exposure time, as shown in Figure 20b. In addition, the average (mean) intensity ratio increases even more than for the Tikhonov regularization. Only for large exposure times (>2 ms) ART and MART will converge towards the values of the Tikhonov regularization and of the radon projections. Thus, a quantitative interpretation of the reconstructed distribution is for ART or MART even more troublesome than for the Tikhonov regularization, especially under conditions with a low signal-to-noise ratio. This emphasizes the indispensable need to characterize the signal-to-noise ratio under the actual experimental conditions in order to be able to reliably assess the quality of the tomographic reconstruction.

5. Conclusions

We presented a novel 2D planar emission tomographic setup (POET$^\lambda$) for the simultaneous detection of multiple species using a single image intensified CCD camera. The alignment, spatial resolution and multispecies detection have been validated against premixed flat flames and laminar diffusion flames in which the distributions of OH*, CH* and soot are a priori known. Subsequently, the new tomographic setup has been successfully used for the simultaneous detection of OH* (310 nm), CH* (430 nm) and soot (750 nm) in non-sooting turbulent methane/air and sooting ethylene/air diffusion flames. Finally, the evaluation of the intensity ratio I_{OH*}/I_{CH*} allows a spatially

resolved classification of combustion zones with preferably premixed or non-premixed combustion, at least qualitatively.

The high correlation coefficient between the simultaneously detected OH* and CH* distributions indicates that our tomographic approach very likely detects the flame structure correctly and that it is not dominated by reconstruction artifacts (see Part II for more details [60]). However, a quantitative interpretation of instantaneous reconstructed intensities (single shot results) has a much greater uncertainty than the flame front position, because the absolute error in the reconstructed intensity is larger compared to the spatial location at which a non-zero intensity (flame front) is observed. Future work will be dedicated to improving the absolute accuracy, for example by amending the alignment procedure. This will be accompanied by a detailed analysis of the effect of an increased number of projection angles on the absolute error in the reconstructed intensities. A major drawback of any tomographic measurement on turbulent flames reported in the literature so far is the subpar spatial resolution compared to, for example, planar laser-induced fluorescence. Due to the very low chemiluminescence intensity of individual species in general, and in combination with our single camera detection scheme based on small numerical apertures for signal detection in our case, the spatial resolution that can be achieved must always be weighed against the time resolution required for investigations in turbulent flow fields.

However, the multiwavelength approach presented here is not limited to chemiluminescent species, soot or combustion systems in general, but can be easily adapted to other spectral regions of interest or systems or it can be combined with, for example, the simultaneous tomographic detection of laser-induced fluorescence of selected or multiple species at very low concentration levels. Furthermore, the camera can easily be exchanged for a camera that is optimized for a different spectral range or that enables recordings with a repetition rate of 1 kHz or more. Besides combustion applications, this offers the possibility to apply the technique to different fields in mechanical engineering. For example, by using spectroscopic lamps in combination with appropriate molecular tracers, added to a flow at a low concentration (ppb level), mixing processes can be monitored or chemical reaction processes can be controlled on-line with very high temporal resolution using real-time tomographic techniques.

Conflicts of Interest: The authors declare no conflict of interest. The funders had no role in the design of the study; in the collection, analyses, or interpretation of data; in the writing of the manuscript, or in the decision to publish the results.

References

1. Gaydon, A.G. *The Spectroscopy of Flames*, 2nd ed.; Springer: Dordrecht, The Netherlands, 1974; ISBN 9789400957220.
2. Hardalupas, Y.; Orain, M. Local measurements of the time-dependent heat release rate and equivalence ratio using chemiluminescent emission from a flame. *Combust. Flame* **2004**, *139*, 188–207. [CrossRef]
3. Candel, S. Combustion dynamics and control: Progress and challenges. *Proc. Combust. Inst.* **2002**, *29*, 1–28. [CrossRef]

4.　Higgins, B.; McQuay, M.Q.; Lacas, F.; Candel, S. An experimental study on the effect of pressure and strain rate on CH chemiluminescence of premixed fuel-lean methane/air flames. *Fuel* **2001**, *80*, 1583–1591. [CrossRef]

5.　Chou, T.; Patterson, D.J. In-cylinder measurement of mixture maldistribution in a L-head engine. *Combust. Flame* **1995**, *101*, 45–57. [CrossRef]

6.　Cheng, T.S.; Wu, C.-Y.; Li, Y.-H.; Chao, Y.-C. Chemiluminescence Measurements of Local Equivalence Ratio in a Partially Premixed Flame. *Combust. Sci. Technol.* **2006**, *178*, 1821–1841. [CrossRef]

7.　Guyot, D.; Guethe, F.; Schuermans, B.; Lacarelle, A.; Paschereit, C.O. CH*/OH* Chemiluminescence Response of an Atmospheric Premixed Flame Under Varying Operating Conditions. In Proceedings of the ASME Turbo Expo 2010: Power for Land, Sea, and Air, Glasgow, UK, 14–18 June 2010; ASME: New York, NY, USA, 2010; pp. 933–944, ISBN 978-0-7918-4397-0.

8.　Ikeda, Y.; Kojima, J.; Nakajima, T. Chemiluminescence based local equivalence ratio measurement in turbulent premixed flames. In Proceedings of the 40th AIAA Aerospace Sciences Meeting & Exhibit, Reno, NV, USA, 14–17 January 2002; American Institute of Aeronautics and Astronautics: Reston, Virigina, 2002; p. 601.

9.　Ikeda, Y.; Kojima, J.; Nakajima, T. Local Chemiluminescence Measurements of OH*, CH* and C2* at Turbulent Premixed Flame-Fronts. In *Smart Control of Turbulent Combustion*; Yoshida, A., Ed.; Springer: Tokyo, Japan, 2001; pp. 12–27. ISBN 978-4-431-66987-6.

10.　McCord, W.; Gragston, M.; Wu, Y.; Zhang, Z.; Hsu, P.; Rein, K.; Jiang, N.; Roy, S.; Gord, J.R. Quantitative fuel-to-air ratio determination for elevated-pressure methane/air flames using chemiluminescence emission. *Appl. Opt.* **2019**, *58*, C61–C67. [CrossRef] [PubMed]

11.　Panoutsos, C.; Hardalupas, Y.; Taylor, A. Numerical evaluation of equivalence ratio measurement using OH* and CH* chemiluminescence in premixed and non-premixed methane–air flames. *Combust. Flame* **2009**, *156*, 273–291. [CrossRef]

12.　Tripathi, M.M.; Krishnan, S.R.; Srinivasan, K.K.; Yueh, F.-Y.; Singh, J.P. Chemiluminescence-based multivariate sensing of local equivalence ratios in premixed atmospheric methane–air flames. *Fuel* **2012**, *93*, 684–691. [CrossRef]

13.　Orain, M.; Hardalupas, Y. Measurements of local mixture fraction of reacting mixture in swirl-stabilised natural gas-fuelled burners. *Appl. Phys. B* **2011**, *105*, 435–449. [CrossRef]

14.　Balachandran, R.; Ayoola, B.; Kaminski, C.; Dowling, A.; Mastorakos, E. Experimental investigation of the nonlinear response of turbulent premixed flames to imposed inlet velocity oscillations. *Combust. Flame* **2005**, *143*, 37–55. [CrossRef]

15.　Ayoola, B.O.; Balachandran, R.; Frank, J.H.; Mastorakos, E.; Kaminski, C.F. Spatially resolved heat release rate measurements in turbulent premixed flames. *Combust. Flame* **2006**, *144*, 1–16. [CrossRef]

16.　Kauranen, P.; Andersson-Engels, S.; Svanberg, S. Spatial mapping of flame radical emission using a spectroscopic multi-colour imaging system. *Appl. Phys. B* **1991**, *53*, 260–264. [CrossRef]

17.　Akamatsu, F.; Wakabayashi, T.; Tsushima, S.; Katsuki, M.; Mizutani, Y.; Ikeda, Y.; Kawahara, N.; Nakajima, T. The development of a light-collecting probe with high spatial resolution applicable to randomly fluctuating combustion fields. *Meas. Sci. Technol.* **1999**, *10*, 1240. [CrossRef]

18.　Aleiferis, P.G.; Hardalupas, Y.; Taylor, A.M.K.P.; Ishii, K.; Urata, Y. Flame chemiluminescence studies of cyclic combustion variations and air-to-fuel ratio of the reacting mixture in a lean-burn stratified-charge spark-ignition engine. *Combust. Flame* **2004**, *136*, 72–90. [CrossRef]

19.　Kojima, J.; Ikeda, Y.; Nakajima, T. Spatially resolved measurement of OH*, CH*, and C2* chemiluminescence in the reaction zone of laminar methane/air premixed flames. *Proc. Combust. Inst.* **2000**, *28*, 1757–1764. [CrossRef]

20.　Anikin, N.B.; Suntz, R.; Bockhorn, H. Tomographic reconstruction of 2D-OH*-chemiluminescence distributions in turbulent diffusion flames. *Appl. Phys. B* **2012**, *107*, 591–602. [CrossRef]

21.　Anikin, N.B.; Suntz, R.; Bockhorn, H. Tomographic reconstruction of the OH*-chemiluminescence distribution in premixed and diffusion flames. *Appl. Phys. B* **2010**, *100*, 675–694. [CrossRef]

22.　Lv, L.; Tan, J.; Hu, Y. Numerical and Experimental Investigation of Computed Tomography of Chemiluminescence for Hydrogen-Air Premixed Laminar Flames. *Int. J. Aerosp. Eng.* **2016**, *2016*, 1–10. [CrossRef]

23. Floyd, J.; Geipel, P.; Kempf, A.M. Computed Tomography of Chemiluminescence (CTC): Instantaneous 3D measurements and Phantom studies of a turbulent opposed jet flame. *Combust. Flame* **2011**, *158*, 376–391. [CrossRef]

24. Floyd, J.; Kempf, A.M. Computed Tomography of Chemiluminescence (CTC): High resolution and instantaneous 3-D measurements of a Matrix burner. *Proc. Combust. Inst.* **2011**, *33*, 751–758. [CrossRef]

25. Geraedts, B.D.; Arndt, C.M.; Steinberg, A.M. Rayleigh Index Fields in Helically Perturbed Swirl-Stabilized Flames Using Doubly Phase Conditioned OH* Chemiluminescence Tomography. *Flow Turbul. Combust.* **2016**, *96*, 1023–1038. [CrossRef]

26. Halls, B.R.; Hsu, P.S.; Roy, S.; Meyer, T.R.; Gord, J.R. Two-color volumetric laser-induced fluorescence for 3D OH and temperature fields in turbulent reacting flows. *Opt. Lett.* **2018**, *43*, 2961–2964. [CrossRef]

27. Halls, B.R.; Hsu, P.S.; Jiang, N.; Legge, E.S.; Felver, J.J.; Slipchenko, M.N.; Roy, S.; Meyer, T.R.; Gord, J.R. kHz-rate four-dimensional fluorescence tomography using an ultraviolet-tunable narrowband burst-mode optical parametric oscillator. *Optica* **2017**, *4*, 897. [CrossRef]

28. Hossain, M.M.; Lu, G.; Yan, Y. Optical Fiber Imaging Based Tomographic Reconstruction of Burner Flames. *IEEE Trans. Instrum. Meas.* **2012**, *61*, 1417–1425. [CrossRef]

29. Hossain, M.M.; Lu, G.; Yan, Y. Three-dimensional reconstruction of combustion flames through optical fiber sensing and CCD imaging. In Proceedings of the IEEE Instrumentation and Measurement Technology Conference (I2MTC), Hangzhou, China, 10–12 May 2011; IEEE: Piscataway, NJ, USA, 2011; pp. 1–5, ISBN 978-1-4244-7933-7.

30. Li, T.; Pareja, J.; Fuest, F.; Schütte, M.; Zhou, Y.; Dreizler, A.; Böhm, B. Tomographic imaging of OH laser-induced fluorescence in laminar and turbulent jet flames. *Meas. Sci. Technol.* **2018**, *29*, 15206. [CrossRef]

31. Li, X.; Ma, L. Capabilities and limitations of 3D flame measurements based on computed tomography of chemiluminescence. *Combust. Flame* **2015**, *162*, 642–651. [CrossRef]

32. Liu, H.; Sun, B.; Cai, W. kHz-rate volumetric flame imaging using a single camera. *Opt. Commun.* **2019**, *437*, 33–43. [CrossRef]

33. Liu, H.; Wang, Q.; Cai, W. Parametric study on single-camera endoscopic tomography. *J. Opt. Soc. Am. B JOSAB* **2020**, *37*, 271–278. [CrossRef]

34. Liu, H.; Zhao, J.; Shui, C.; Cai, W. Reconstruction and analysis of non-premixed turbulent swirl flames based on kHz-rate multi-angular endoscopic volumetric tomography. *Aerosp. Sci. Technol.* **2019**, *91*, 422–433. [CrossRef]

35. Ma, L.; Wu, Y.; Lei, Q.; Xu, W.; Carter, C.D. 3D flame topography and curvature measurements at 5 kHz on a premixed turbulent Bunsen flame. *Combust. Flame* **2016**, *166*, 66–75. [CrossRef]

36. Ruan, C.; Chen, F.; Cai, W.; Qian, Y.; Yu, L.; Lu, X. Principles of non-intrusive diagnostic techniques and their applications for fundamental studies of combustion instabilities in gas turbine combustors: A brief review. *Aerosp. Sci. Technol.* **2019**, *84*, 585–603. [CrossRef]

37. Unterberger, A.; Röder, M.; Giese, A.; Al-Halbouni, A.; Kempf, A.M.; Mohri, K. 3D Instantaneous Reconstruction of Turbulent Industrial Flames Using Computed Tomography of Chemiluminescence (CTC). *J. Combust.* **2018**, *2018*, 1–6. [CrossRef]

38. Unterberger, A.; Kempf, A.M.; Mohri, K. 3D Evolutionary Reconstruction of Scalar Fields in the Gas-Phase. *Energies* **2019**, *12*, 2075. [CrossRef]

39. Wang, J.; Song, Y.; Li, Z.-H.; Kempf, A.M.; He, A.-Z. Multi-directional 3D flame chemiluminescence tomography based on lens imaging. *Opt. Lett.* **2015**, *40*, 1231–1234. [CrossRef]

40. Wang, J.; Zhang, W.; Zhang, Y.; Yu, X. Camera calibration for multidirectional flame chemiluminescence tomography. *Opt. Eng.* **2017**, *56*, 41307. [CrossRef]

41. Wang, K.; Li, F.; Zeng, H.; Yu, X. Three-dimensional flame measurements with large field angle. *Opt. Express* **2017**, *25*, 21008. [CrossRef]

42. Wiseman, S.M.; Brear, M.J.; Gordon, R.L.; Marusic, I. Measurements from flame chemiluminescence tomography of forced laminar premixed propane flames. *Combust. Flame* **2017**, *183*, 1–14. [CrossRef]

43. Worth, N.A.; Dawson, J.R. Tomographic reconstruction of OH* chemiluminescence in two interacting turbulent flames. *Meas. Sci. Technol.* **2013**, *24*, 24013. [CrossRef]

44. Yu, T.; Ruan, C.; Chen, F.; Wang, Q.; Cai, W.; Lu, X. Measurement of the 3D Rayleigh index field via time-resolved CH* computed tomography. *Aerosp. Sci. Technol.* **2019**, 105487. [CrossRef]

45. Yu, T.; Ruan, C.; Liu, H.; Cai, W.; Lu, X. Time-resolved measurements of a swirl flame at 4 kHz via computed tomography of chemiluminescence. *Appl. Opt.* **2018**, *57*, 5962. [CrossRef]

46. Denisova, N. Plasma Diagnostics Using Computed Tomography Method. *IEEE Trans. Plasma Sci.* **2009**, *37*, 502–512. [CrossRef]

47. Goyal, A.; Chaudhry, S.; Subbarao, P.M.V. Direct three dimensional tomography of flames using maximization of entropy technique. *Combust. Flame* **2014**, *161*, 173–183. [CrossRef]

48. Song, J.; Hong, Y.; Wang, G.; Pan, H. Algebraic tomographic reconstruction of two-dimensional gas temperature based on tunable diode laser absorption spectroscopy. *Appl. Phys. B* **2013**, *112*, 529–537. [CrossRef]

49. Wang, K.; Li, F.; Zeng, H.; Zhang, S.; Yu, X. Computed tomography measurement of 3D combustion chemiluminescence using single camera. In Proceedings of the International Symposium on Optoelectronic Technology and Application 2016, Beijing, China, 9–11 May 2016; p. 1015531.

50. Yu, T.; Liu, H.; Cai, W. On the quantification of spatial resolution for three-dimensional computed tomography of chemiluminescence. *Opt. Express* **2017**, *25*, 24093–24108. [CrossRef]

51. Pareja, J.; Johchi, A.; Li, T.; Dreizler, A.; Böhm, B. A study of the spatial and temporal evolution of auto-ignition kernels using time-resolved tomographic OH-LIF. *Proc. Combust. Inst.* **2019**, *37*, 1321–1328. [CrossRef]

52. Atkinson, C.; Soria, J. Algebraic Reconstruction Techniques for Tomographic Particle Image Velocimetry. In Proceedings of the 16th Australasian Fluid Mechanics Conference, Crown Plaza, Gold Coast, Australia, 2–7 December 2007.

53. Atkinson, C.; Soria, J. An efficient simultaneous reconstruction technique for tomographic particle image velocimetry. *Exp. Fluids* **2009**, *47*, 553–568. [CrossRef]

54. Elsinga, G.E.; Scarano, F.; Wieneke, B.; van Oudheusden, B.W. Tomographic particle image velocimetry. *Exp. Fluids* **2006**, *41*, 933–947. [CrossRef]

55. Scarano, F. Tomographic PIV: Principles and practice. *Meas. Sci. Technol.* **2013**, *24*, 12001. [CrossRef]

56. Atkinson, C.; Coudert, S.; Foucaut, J.-M.; Stanislas, M.; Soria, J. The accuracy of tomographic particle image velocimetry for measurements of a turbulent boundary layer. *Exp. Fluids* **2011**, *50*, 1031–1056. [CrossRef]

57. Kathrotia, T.; Riedel, U.; Seipel, A.; Moshammer, K.; Brockhinke, A. Experimental and numerical study of chemiluminescent species in low-pressure flames. *Appl. Phys. B* **2012**, *107*, 571–584. [CrossRef]

58. De Leo, M.; Saveliev, A.; Kennedy, L.; Zelepouga, S. OH and CH luminescence in opposed flow methane oxy-flames. *Combust. Flame* **2007**, *149*, 435–447. [CrossRef]

59. Dandy, D.S.; Vosen, S.R. Numerical and Experimental Studies of Hydroxyl Radical Chemiluminescence in Methane-Air Flames. *Combust. Sci. Technol.* **1992**, *82*, 131–150. [CrossRef]

60. Häber, T.; Suntz, R.; Bockhorn, H. Two-dimensional tomographic simultaneous multi-species visualization—Part II: Reconstruction Accuracy. *Energies* **2020**, Submitted.

61. Mullaney, J. (Ed.) *The Herschel Objects, and How to Observe Them*; Springer: New York, NY, USA, 2007; ISBN 978-0-387-68124-5.

62. Häber, T.; Gebretsadik, M.; Bockhorn, H.; Zarzalis, N. The effect of total reflection in PLIF imaging of annular thin films. *Int. J. Multiph. Flow* **2015**, *76*, 64–72. [CrossRef]

63. Malitson, I.H. Interspecimen Comparison of the Refractive Index of Fused Silica. *J. Opt. Soc. Am.* **1965**, *55*, 1205. [CrossRef]

64. Daun, K.J.; Grauer, S.J.; Hadwin, P.J. Chemical species tomography of turbulent flows: Discrete ill-posed and rank deficient problems and the use of prior information. *J. Quant. Spectrosc. Radiat.* **2016**, *172*, 58–74. [CrossRef]

65. Daun, K.J. Infrared species limited data tomography through Tikhonov reconstruction. *J. Quant. Spectrosc. Radiat.* **2010**, *111*, 105–115. [CrossRef]

66. Hadamard, J. Sur les problèmes aux dérivées partielles et leur signification physique. *Princet. Univ. Bull.* **1902**, *13*, 49–52.

67. Hansen, P.C. *Rank-Deficient and Discrete Ill-Posed Problems*; Society for Industrial and Applied Mathematics: Philadelphia, PA, USA, 1998; ISBN 978-0-89871-403-6.

68. Tikhonov, A.N.; Arsenin, V.I. *Solutions of Ill-Posed Problems. Andrey N. Tikhonov and Vasiliy Y. Arsenin. Translation Editor Fritz John*; Wiley: New York, NY, USA, 1977; ISBN 9780470991244.

69. Jing, L.; Liu, S.; Zhihong, L.; Meng, S. An image reconstruction algorithm based on the extended Tikhonov regularization method for electrical capacitance tomography. *Measurement* **2009**, *42*, 368–376. [CrossRef]

70. Dodge, Y.; Jurečková, J. *Adaptive Regression*; Springer: New York, NY, USA, 2000; ISBN 9780387989655.

71. Hong, M.; Yu, Y.; Wang, H.; Liu, F.; Crozier, S. Compressed sensing MRI with singular value decomposition-based sparsity basis. *Phys. Med. Biol.* **2011**, *56*, 6311–6325. [CrossRef]

72. Zdunek, R. Multigrid Regularized Image Reconstruction for Limited-Data Tomography. *CMST* **2007**, *13*, 67–77. [CrossRef]

73. Lewis, J.P. Fast Normalized Cross-Correlation. In Proceedings of the Vision Interface, Québec, QC, Canada, 16–19 May 1995.

74. Wang, Z.; Bovik, A.C.; Sheikh, H.R.; Simoncelli, E.P. Image quality assessment: From error visibility to structural similarity. *IEEE Trans. Image Process.* **2004**, *13*, 600–612. [CrossRef] [PubMed]

75. Wang, H.; Kook, S.; Doom, J.; Oefelein, J.C.; Zhang, J.; Shaddix, C.R.; Schefer, R.W.; Pickett, L.M. *Understanding and Predicting Soot Generation in Turbulent non-Premixed Jet Flames*; Technical Report SAND2010-7178; Sandia National Laboratories: Albuquerque, NM, USA, 2010.

76. Lee, S.-Y.; Turns, S.R.; Santoro, R.J. Measurements of soot, OH, and PAH concentrations in turbulent ethylene/air jet flames. *Combust. Flame* **2009**, *156*, 2264–2275. [CrossRef]

77. García-Armingol, T.; Ballester, J.; Smolarz, A. Chemiluminescence-based sensing of flame stoichiometry: Influence of the measurement method. *Measurement* **2013**, *46*, 3084–3097. [CrossRef]

78. Gordon, R.; Bender, R.; Herman, G.T. Algebraic Reconstruction Techniques (ART) for three-dimensional electron microscopy and X-ray photography. *J. Theor. Biol.* **1970**, *29*, 471–481. [CrossRef]

79. Herman, G.T.; Lent, A. Iterative reconstruction algorithms. *Comput. Biol. Med.* **1976**, *6*, 273–294. [CrossRef]

80. Mailloux, G.E.; Noumeir, R.; Lemieux, R. Deriving the multiplicative algebraic reconstruction algorithm (MART) by the method of convex projection (POCS). In Proceedings of the ICASSP '93, IEEE International Conference on Acoustics, Speech, and Signal Processing, Minneapolis, MN, USA, 27–30 April 1993; Volume 5, pp. 457–460, ISBN 0-7803-0946-4.

81. De Pierro, A.R. Multiplicative iterative methods in computed tomography. In *Mathematical Methods in Tomography, Proceedings of the Conference held in Oberwolfach, Germany, 5–11 June 1990*; Herman, G.T., Louis, A.K., Natterer, F., Eds.; Springer: Berlin, Germany, 1991; pp. 167–186. ISBN 978-3-540-54970-3.

82. Hunter, J.D. Matplotlib: A 2D graphics environment. *Comput. Sci. Eng.* **2007**, *9*, 90–95. [CrossRef]

83. Ramachandran, P.; Varoquaux, G. Mayavi: 3D Visualization of Scientific Data. *Comput. Sci. Eng.* **2011**, *13*, 40–51. [CrossRef]